

Packing simulations of complex-shaped rigid particles using FDEM: An application to catalyst pellets



Ado Farsi ^{a,*}, Jiansheng Xiang ^a, John-Paul Latham ^a, Mikeal Carlsson ^b, Hugh Stitt ^b, Michele Marigo ^b

^a Applied Modelling and Computation Group, Department of Earth Science and Engineering, Imperial College London, South Kensington Campus, London SW7 2AZ, United Kingdom

^b Johnson Matthey, P.O. Box 1, Belasis Avenue, Billingham, Cleveland TS23 1LB, United Kingdom

ARTICLE INFO

Article history:

Received 3 July 2020

Received in revised form 10 October 2020

Accepted 9 November 2020

Available online 13 November 2020

Keywords:

Combined finite-discrete element method

Packing density

Fixed-bed reactors

Particle technology

Ceramics

ABSTRACT

A new component of the combined finite-discrete element method (FDEM) is employed to estimate the effects of geometrical features, friction and energy dissipation parameters on the bulk properties of rigid pellet packs. This work constitutes the first systematic validation of the Solidity FDEM code for rigid particles. The experimental and numerical axial and radial packing density profiles and orientation distributions have been compared, confirming that the numerical simulations of packing of cylindrical catalyst supports, glass beads and trilobe pellets deposited in a cylindrical container match the corresponding emergent bulk properties obtained from X-Ray CT scans. The presented results are a first confirmation of the applicability of FDEM based methods to the simulation of this class of multi-body problems. The assessment of the accuracy of the simulated topology of the pellet pack that is established in this work is encouraging for further investigations of the multi-physical engineering systems of interest for catalyst pellets involving hydro-thermo-mechanical, fracturing and fragmentation interactions using coupled FDEM formulations.

© 2020 Elsevier B.V. All rights reserved.

1. Introduction

Heterogeneous catalysts are employed in a large number of industrial chemical plants. Catalyst pellets can be extruded or moulded with different shapes: spheres, cylinders, trilobes, etc. These shapes can include internal holes to increase the surface area of the pellets. To design a pellet shape several aspects have to be taken into account: the manufacturing costs, the catalytic efficiency, the tendency to break and increase pressure drops, just to name a few. Other factors to take into account include the loading method used to fill the reactor and the ratio between the container and pellet size.

Pseudohomogenous approaches (i.e. models based on a continuous representation of the packed bed) fail to produce accurate predictions of the behaviour that are used to evaluate fields of interest (e.g. the temperature field) inside fixed-bed reactors, especially for narrow to moderate tube-to-pellet diameter ratios [1]. The aim of improved discontinuous simulations is therefore to create highly accurate descriptions of the void geometry for further heat and flow modelling, as well as to represent more realistic loading conditions that can lead to the crushing of catalyst supports, such as during the shrinkage of the reactor tubes.

Numerous papers address the packing of spherical pellets in a cylindrical container. Nolan and co-authors [2] propose an iterative

algorithm that displaces spheres that are initially randomly located in a cylindrical container, until they reach "gravitational stability" without relative interpenetration. Salvat and co-authors [3] employ a so called "soft spheres algorithm" (that allows some degree of interpenetration between particles) to simulate packs of mono-sized spheres in cylindrical containers. Muller [4] computes the mean and radial packing density of spheres in a cylinder employing a sequential placing algorithm. Caulkin and co-authors [5] discretise the simulated domain with a grid, where the space occupied by the spherical particles and the cylindrical container is defined by voxels. The packing is then calculated with a semi-stochastic approach, where the particle path is randomly determined on the basis of the overlapping of voxels.

Recently, simulations of spherical bodies have been used for the modelling of pebble beds in [6]. The effects of the packing structure on the effective thermal conductivity have been modelled in [7]. The packing structure, container shape and structure-indices relations have also been investigated with multi-body simulations of spherical particles. In particular, the boundary/wall effects on the pack of spheres have been investigated in [8,9], comparing both numerical simulations and x-ray scans.

On the other hand, the literature dealing with non-spherical pellets has been scarce until recently. In [10,11] the packing process is simulated with both a semi-stochastic approach, where the particle path is randomly determined on the basis of the overlapping of voxels (DigiCGP), and a deterministic approach, where the repulsive forces and torques applied to the particles are calculated by measuring the

* Corresponding author.

E-mail address: ado.farsi@imperial.ac.uk (A. Farsi).

number of their overlapping voxels and their voxel-level contact forces (DigiDEM). Boccardo and Partopour [12,13] use the discrete element method (DEM) implemented in Blender [14]. Dorai, Wachs and co-authors [15–17] employ a variant to DEM with the GilbertJohnsonKeerthi algorithm to compute the distance between non-spherical convex particles. A so called rigid dynamics algorithm is used in [18], where the transition between moving and resting perfectly rigid particles is controlled by a cutoff on the relative contact velocities, instead of employing the contact stiffness and damping used in DEM based codes.

A combined finite-discrete element method (FDEM) has been employed for the evaluation of the strength of individual catalyst pellets for simplified loading conditions [19–21]. To allow the representation of more realistic pellet loading and tube filling conditions the whole packed structure of catalysts in fixed-bed reactors need to be correctly captured in the simulation. The capabilities of FDEM codes for the simulation of packed structures of catalysts in fixed-bed reactors therefore need to be assessed for both the creation of the void topology associated with the solid skeleton and the accurate creation of contact loading on individual pellets. In either case, the problem begins with simulating the packing of pellets.

In this context, a validation study for the simulation of rigid particles with a FDEM code is presented in this work, where the focus is on reproducing experimental packing results when pellets are released into cylindrical containers. The final aim of this work is to verify the capabilities of the FDEM framework for the accurate representation of pack structures of systems of complex-shaped pellets. This constitutes the first and a necessary step for the application of the code to other coupled systems, such as involving fluid and thermal interactions, stress, deformation and fragmentation of packing structures.

To highlight the capabilities of FDEM methods for the simulation of stresses and deformations in the pack of catalyst supports, the simulated stress chains resulting from a gentle compression of a pack of cylinders is shown in Fig. 1 [22]. Rather than simulate both the packing and compaction processes with deformable FDEM, the most efficient

workflow is as follows. First, harness the rigid component of the FDEM code to simulate the packing process for which the rigid assumption is excellent. The rigid component of the FDEM code is the main subject of this paper. Second, apply the deformable component of the FDEM code to enable the rigid body packing structure to make fine adjustments to form its new equilibrium state, taking account of the realistic elastic parameters for catalyst supports from [23]. Finally, simulate a gentle vertical compaction to illustrate the calculation of local stress concentrations and deformations of catalyst supports. These preliminary simulation results show how stress chains and vulnerability to crushing or tensile fracture might be examined by analysing different stress components from the output of FDEM simulations.

The history of particle entry and coalescence (e.g. entry rate and velocity) can influence the final pack in terms of spacing and the randomness of the orientation. As has been pointed out in [24], regular deposition grids of particles and with random orientations tended to generate packed structures with artificial regularities. For this reason in this work the particles are introduced into the domain inside the container in a random irregular grid from a fixed height, with random orientations. It is worth mentioning that the literature has a considerable number of recommended procedures to generate random orientations, but when implemented show a marked lack of randomness. Moghaddam and co-author have recently shown in [18] the role of the loading methods and filling speed in the final topology of the pack pellets. Although more research needs to be carried out to study in detail the relation between feeding conditions and properties of the obtained packed structures and to design a range of new improved deposition algorithms that can be recommended for different practical cases of particle entry, this has not been the focus of the current work.

Packing simulations with DEM are normally employed to estimate the packing density and topological structure. As summarised in [25], in order to characterise natural and industrial packed structures emergent properties of the pack are normally inferred from simulation results. For the same reason, these emergent bulk properties, i.e. axial and radial packing density profiles, pellet orientation distributions,

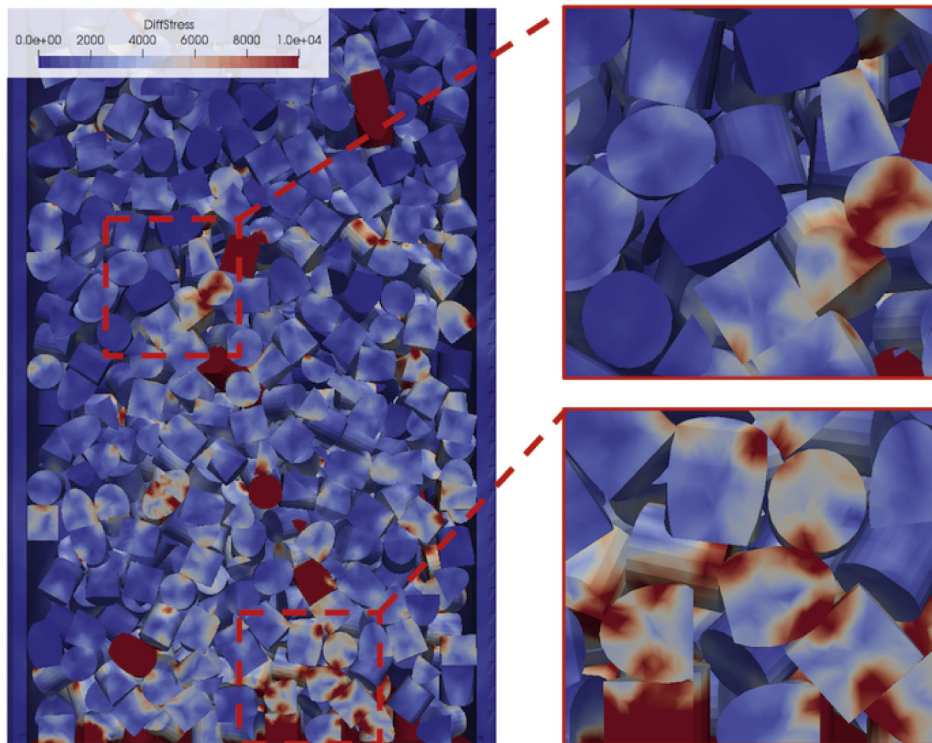


Fig. 1. Differential stress in a vertical cross section of the 3D pack of cylindrical pellets in a cylindrical container [22].

etc., are the quantities that are employed for packing simulations validations in previous publications and in the current work. The potentially confusing term "vertical orientation distributions" has been used in previous works (e.g. [10,11]) to describe the statistics of the angles between the principal axis of the pellets and the vertical axis of the container. The way in which these statistics, and the other packing property descriptors, are calculated in this work are described in the Appendices. To help the reader compare the results that are presented here with the relevant literature, the same term "vertical orientation distributions" has also been used in this work.

After introducing the key aspects of the FDEM technology in Section 2, this paper describes the computational models that have been used for the packing simulations in Section 3. A study of the effects of the mesh resolution, contact, friction and energy dissipation parameters on the bulk properties of cylindrical pellet packs is shown in Section 4. The comparison between the numerical results and experimental X-Ray CT scans for packs of cylinders, spheres and trilobes is shown in Section 4.6 and Section 5.

2. FDEM theory

Algorithms for FDEM simulations started to be proposed from the 90s. Developments and applications of the FDEM method have been carried out after the release of the open source Y-code in [26] by Munjiza. Modelling methods that can accommodate the effect of shape on packing, including DEM and FDEM, were summarised in a recent publication [27], where the class of particulate problems that are well-suited to FDEM are presented and discussed. Imperial College London, in a collaboration with Queen Mary University of London, released the first open source FDEM code for geoscience problems in the late 2000s [28]. This code, initially named Virtual Geoscience Simulation Tools (VGeST), has been recently upgraded to simulate more general mechanical problems and renamed 'Solidity' [29,30]. The key features of FDEM are the following: (a) compute the contact interactions and motion of bodies, (b) calculate the stresses and deformations and (c) compute the transition from continua to discontinua when fragmentation occurs. Since in this work the pellets and the containers are simulated as rigid bodies, the focus of this section will be mainly on the calculation of the contact forces and the computation of the trajectories of the simulated bodies. Details on the theoretical underpinnings of the algorithms used to calculate the stresses and trajectories of deformable bodies will be also introduced in this section. More background on the original and novel implementations of smeared crack model in FDEM can be found in [31,32]. Some details on the feasibility of the algorithm in practical applications are discussed in [33]. Further details of the algorithms that have been used for this work are covered in a separate paper that is currently in preparation.

2.1. Contact interactions

In FDEM all simulated bodies are discretised with a finite-element mesh. When two bodies are in contact, some of the elements of the mesh of the two bodies overlap. A contact detection algorithm detects all the couples of elements that are more likely to be in contact, discarding all the couples that are too far to be in contact. This is done to avoid processing the contact interaction of all the possible couple of elements in the system and therefore reducing the run time of the simulation. The contact interaction is implemented through a variational formulation. The penalty function method is used to compute the normal component of the contact force between two bodies by imposing the stationarity of a functional subject to the contact constraints over the boundaries. The contact potential function is defined in the form of Eq. (1), where PT is the penalty term, while $f(\mathbf{p})$ is a function of the point \mathbf{p} in the overlapping elements of the two contacting bodies. The function $f(\mathbf{p})$ is defined in such a way that it is zero outside the discrete

element, constant on the boundaries and increasing while moving towards the centre of the elements.

$$\varphi(\mathbf{p}) = PT \cdot f(\mathbf{p}) \quad (1)$$

The infinitesimal contact force is defined as the gradient of the corresponding potential function $d\mathbf{F} = -\nabla\varphi dV$, where dV is the infinitesimal overlapping volume. The total contact force can then be calculated by integrating the infinitesimal contact force field over the overlapping volume, as shown in Eq. 2, where β_t and β_c are the target and contactor bodies in contact. This ensures that the energy during the contact interaction is conserved, independently of the penalty term, element shape or magnitude of the penetration, as the so-defined contact force field is conservative.

$$\mathbf{f}_{cn} = \int_{V=\beta_t \cap \beta_c} [\nabla\varphi_c - \nabla\varphi_t] dV \quad (2)$$

By replacing integration over the overlapping volumes with the integral over the boundaries of the overlapping volumes, see [34], the total normal contact force \mathbf{f}_{cn} can be calculated with Eq. (3), where \mathbf{n} is the outward unit normal to the surface of the overlapping volume of the two bodies in contact.

$$\mathbf{f}_{cn} = \int_{S_{\beta_t \cap \beta_c}} \mathbf{n}(\varphi_c - \varphi_t) dA \quad (3)$$

Since both the target and contactor bodies in contact are discretised with finite elements, each body can be represented as the union of its finite elements, as shown in Eq. 4. The indexes m and n are the total number of finite elements of the contactor and target respectively. The potentials φ_c and φ_t can also be expressed as the sum of potentials associated with each finite element, as shown in Eq. (5).

$$\begin{aligned} \beta_c &= \beta_{c_1} \cup \beta_{c_2} \dots \cup \beta_{c_n} \\ \beta_t &= \beta_{t_1} \cup \beta_{t_2} \dots \cup \beta_{t_m} \end{aligned} \quad (4)$$

$$\begin{aligned} \varphi_c &= \varphi_{c_1} \cup \varphi_{c_2} \dots \cup \varphi_{c_n} \\ \varphi_t &= \varphi_{t_1} \cup \varphi_{t_2} \dots \cup \varphi_{t_m} \end{aligned} \quad (5)$$

By replacing the integral over the boundaries of the overlapping volumes of Eq. (3) with the summation of the integration over the finite element boundaries, the total normal contact force \mathbf{f}_{cn} can be calculated with Eq. 6. In this way the contact force between overlapping bodies is calculated by summation over the surfaces of the corresponding overlapping finite elements.

$$\mathbf{f}_{cn} = \sum_{i=1}^n \sum_{j=1}^m \int_{S_{\beta_{c_i} \cap \beta_{t_j}}} \mathbf{n}(\varphi_{c_i} - \varphi_{t_j}) dS \quad (6)$$

Since the solution obtained through the minimisation of the potential function satisfies the constraint of impenetrability only approximately, the contacting couples tend to penetrate into each other, generating distributed contact forces along their boundaries. With a sufficiently large penalty term (PT) the extent of the overlapping is negligible as is the related error in the response of the simulated system. In the case of deformable bodies, the difference between the effects of two different but statically equivalent loads becomes very small at sufficiently large distances from load, see [35], therefore the structural response of a body to contact forces can be well represented even though the mesh discretisation and penalty term might locally influence the correct distribution of the pressure on the contact surfaces of two colliding bodies.

The tangential contact force, or sliding frictional force formulation is based on the Coulomb model of friction. This force is calculated with Eq. (7), where FC is the sliding friction coefficient, \mathbf{d}_t is the tangential

Table 1

Geometries of the pellets and containers that have been used in [37,38] and simulated in this work.

	Pellet diameter [mm]	Pellet length [mm]	Pellet equivalent diameter [mm]	Container diameter [mm]
Cylinders	3.42	3.46	3.9	44.5
Spheres	2		2	19
Trilobes	1.3	4	2	19

displacement vector and k_t is the tangential contact stiffness (normally set to $0.1 * PT$).

$$\begin{cases} \mathbf{f}_{ct} = -k_t \mathbf{d}_t & \text{for } |\mathbf{f}_{ct}| \leq FC|\mathbf{f}_{cn}| \\ \mathbf{f}_{ct} = -FC |\mathbf{f}_{cn}| \frac{\mathbf{d}_t}{|\mathbf{d}_t|} & \text{for } |\mathbf{f}_{ct}| > FC|\mathbf{f}_{cn}| \end{cases} \quad (7)$$

For deformable bodies, the damping forces are calculated by integrating the portion of the visco-elastic stresses that are proportional to the rate of deformation. In the case of rigid bodies, the damping formulation is similar to the formulation used by Cundall and co-authors in [36,37]. The damping force applied to each particle \mathbf{f}_{cd} is proportional to the constant DC and is given by Eq. (8). The vector \mathbf{F} is the net unbalanced force acting on the body, i.e. the sum of the normal and frictional contact forces ($\mathbf{F} = \mathbf{f}_{cn} + \mathbf{f}_{ct}$). The term $\text{sign}(\mathbf{V})$ is the sign (positive or negative) of the velocity of the body.

$$\mathbf{f}_{cd} = -DC\mathbf{F}\text{sign}(\mathbf{V}) \quad (8)$$

2.2. Motion of bodies

When the bodies are simulated as rigid particles, there are no internal forces acting on the element nodes and the relative displacements between nodes of all the elements belonging the same body is zero. For this reason the governing equation can be rewritten in the form of the dynamic equilibrium equation with respect to the centres of mass of each body. The trajectory of each simulated body can therefore be obtained by integrating over time the dynamic translational and rotational equilibrium equations given by Eq. (9) and Eq. (10).

$$m_{p,i}\ddot{\mathbf{x}}_{p,i} = \mathbf{f}_{d,i} + m_{p,i}\mathbf{g} + \sum_{j=1}^{k_i} (\mathbf{f}_{cn,ij} + \mathbf{f}_{ct,ij} + \mathbf{f}_{cd,ij}) \quad (9)$$

$$\mathbf{I}_{p,i}\ddot{\theta}_{p,i} = \sum_{j=1}^{k_i} \mathbf{T}_{c,ij} \quad (10)$$

where $m_{p,i}$ and $\mathbf{I}_{p,i}$ are the mass and moment of inertia of each body i . $\dot{\mathbf{x}}_{p,i}$ and $\dot{\theta}_{p,i}$ are the linear and angular acceleration of the body i . $\mathbf{T}_{c,ij}$ is torque generated by the normal ($\mathbf{f}_{cn,ij}$) contact forces, frictional forces ($\mathbf{f}_{ct,ij}$) and by the damping forces ($\mathbf{f}_{cd,ij}$). These torques and forces are computed for all the k_i elements j in contact with each body i .

When the deformable components of the FDEM code are employed (e.g. in the simulation in Fig. 1), the coordinates of the nodal points of the elements that discretise the bodies are determined by the dynamic equilibrium of the forces that are acting on the element nodes. These forces are either internal nodal forces (\mathbf{f}_{int}) given by the visco-elastic element deformations or external nodal forces (\mathbf{f}_{ext}). For each element, the internal and external nodal forces are given by Eq. (11) and Eq. (12) respectively [32].

$$\mathbf{f}_{int} = \int_{V_e} \frac{\partial \mathbf{N}}{\partial \mathbf{x}} \sigma dV \quad (11)$$

$$\mathbf{f}_{ext} = \int_{V_e} \mathbf{Nb} dV + \int_{S_e} \mathbf{Nt} dA \quad (12)$$

where \mathbf{N} is the element shape function, σ is the stress tensor, \mathbf{b} is the body force acting on the volume of element and \mathbf{t} is the traction acting on the surface of the element. The trajectory of the simulated bodies can be obtained by integrating over time the dynamic equilibrium equation given by Eq. (13).

$$\mathbf{M}\ddot{\mathbf{x}}_n^T + \mathbf{f}_{int} = \mathbf{f}_{ext} + \mathbf{f}_c \quad (13)$$

where \mathbf{f}_c is the total force that is generated during the contact interactions between different bodies. This is given by the sum of the normal contact force (\mathbf{f}_{cn}) to avoid body interpenetration, and the tangential force (\mathbf{f}_{ct}) due to friction and the damping force (\mathbf{f}_{cd}) due to other forms of energy loss during contact. The nodal mass matrix \mathbf{M} is calculated for each element based on the initial element configuration with Eq. (14), where ρ_0 is the density of the element.

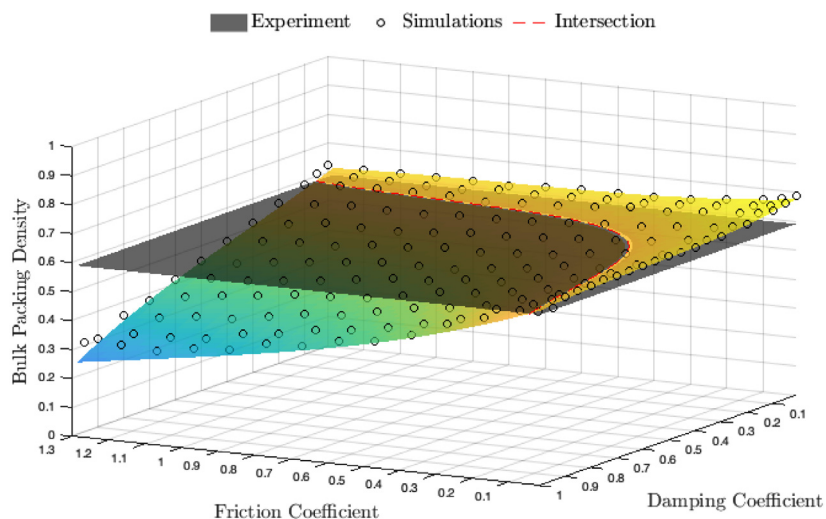


Fig. 2. Parameter space for the friction and damping coefficients: the grey plane corresponds to the bulk packing density (0.591) that was calculated from the physical experiment of cylindrical pellet named A38 in [38]. The black circles correspond to the bulk packing density calculated from 180 numerical simulations with different combinations of the two parameters, and then interpolated with a surface in the parameter space. The red dashed line is the intersection between the experimental plane and the interpolated surface [CY16 - PT 3.5×10^6]. (For interpretation of the references to colour in this figure legend, the reader is referred to the web version of this article.)

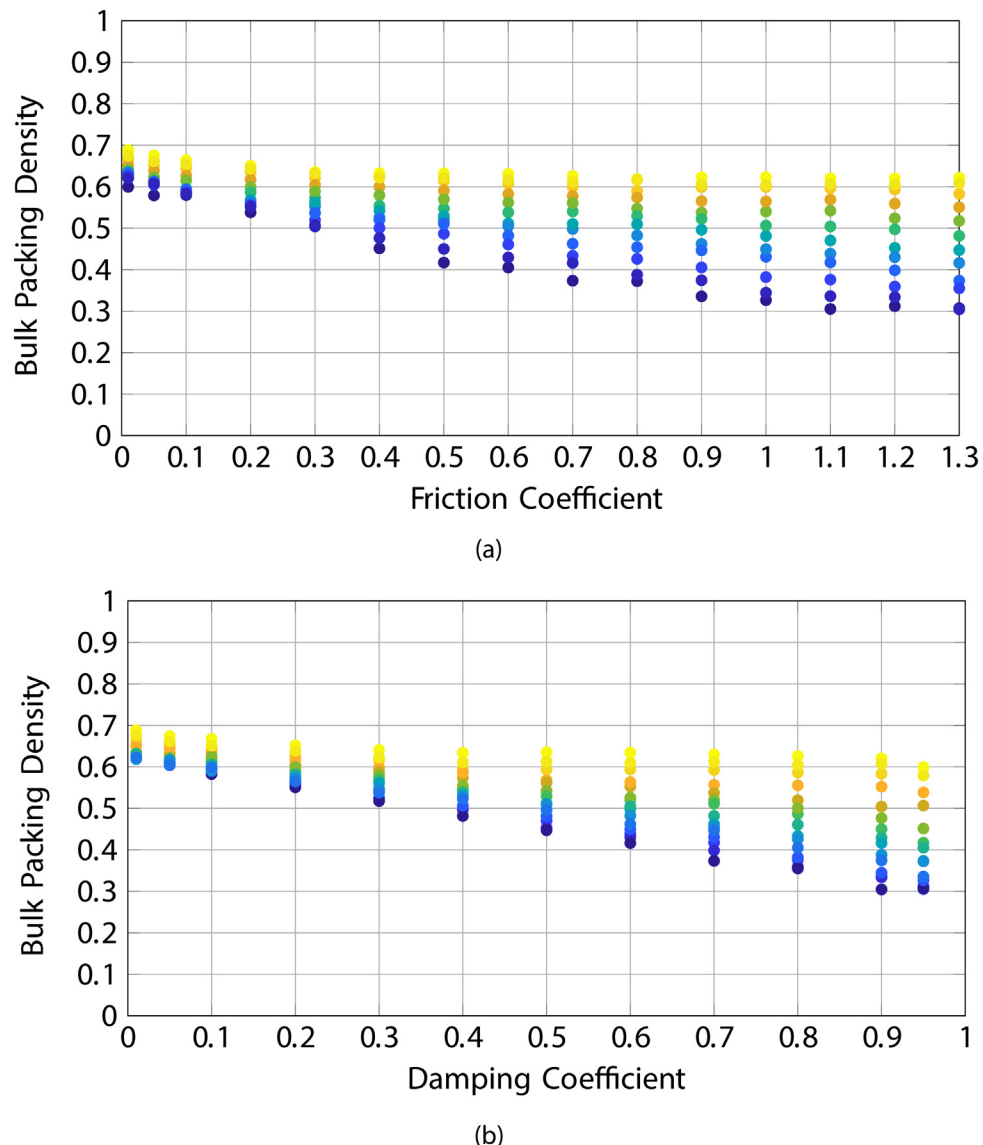


Fig. 3. Effects of friction and damping coefficient on the bulk packing density of cylinders named A38 in [37] deposited into a cylindrical container. a) Bulk packing density against friction coefficient for damping coefficients in the 0.01 (blue) - 0.95 (yellow) range. b) Bulk packing density against damping coefficient for friction coefficients in the 0.01 (blue) - 1.3 (yellow) range [CY16 - PT 3.5×10^6]. (For interpretation of the references to colour in this figure legend, the reader is referred to the web version of this article.)

$$\mathbf{M} = \int_{V_0} \rho_0 \mathbf{N} \mathbf{N}^T dV \quad (14)$$

3. Model setup

Packs of solid cylindrical, spherical and complex-shaped (trilobes) particles are simulated using FDEM. The geometries of cylindrical catalyst support (A38) and their corresponding cylindrical container refer to [37], whereas the geometries of the spheres, trilobes and their corresponding container refer to [38]. All the geometries have been summarised in Table 1. The geometries of complex-shaped bodies and the container itself have been imported from CAD files and then discretised with a tetrahedral mesh, as shown in Fig. 7 and Fig. 20. The contact forces are calculated with the penalty method and the Coulomb model of friction that has been described in the previous sections. The energy loss during impacts is modelled with a damping force

proportional to the particle unbalanced net force during the impact, as described in the previous section.

As has been pointed out in [24], regular deposition grids of particles (i.e. particles with their centres of gravity placed with equal spacing in the two horizontal directions) and with random orientations tended to generate packed structures with artificial regularities. With the purpose of simulating the depositing of pellets in a manner similar to real pouring processes and in ways that can be expected to be highly random, the pre- and post-processing tools have been further improved. This improvement has included the specific task to verify that during the container filling stage, and prior to switching gravity on, particles were generated within the domain with random orientations. Furthermore, a procedure to prevent regular spaced grid locations in a user-defined deposition volume was also implemented. This verification has been carried out first by analysing the orientation distributions on a stereo-net of the generated particles and then by examining the distributions of the coordinates of the centroids. The particles are introduced in the domain above the container base with random orientations and zero initial velocity. This process is completely automated

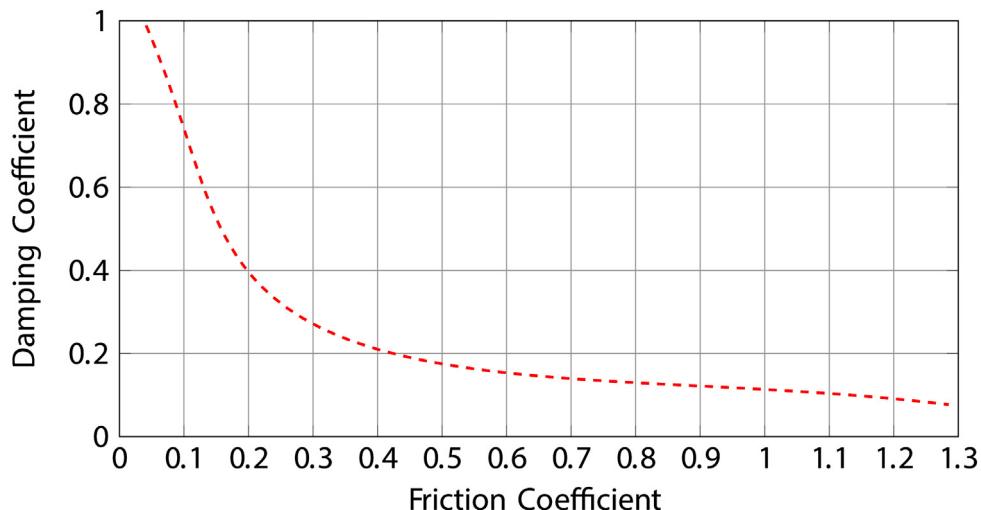


Fig. 4. Optimal combination of friction and damping coefficients to match the experimental data of cylindrical pellet named A38 in [37]. The red dashed line is the intersection between the experimental plane and the interpolated parameter surface in Fig. 2 [CY16 - PT 3.5×10^6]. (For interpretation of the references to colour in this figure legend, the reader is referred to the web version of this article.)

Table 2

Parameters and mesh discretisation used to simulate the packing of A38 catalyst support.

Penalty term	Mesh resolution	Friction coef.	Damping coef.
Min	3.5×10^4	CY04	0.01
Max	3.5×10^6	CY24	1.3
Opt	3.5×10^6	CY16	0.55

through a pre-processing tool that facilitates the control of filling conditions and avoids the need for a manually defined 3D space for the initial conditions of each single pellet. The simulation runs in parallel on 34 cores in less than twenty-four hours. The numerical results are then analysed with a post-processing tool to estimate the axial and radial packing density profiles and the pellet orientation distribution. These post-processing tools are described in the Appendices sections.

The state-of-rest can also be easily visualised and scrutinised with post-processing tools such as Paraview [40].

4. Packing of cylinders

The A38 catalyst support (one specific size and aspect ratio considered by Caulkin and co-workers in their experiments for which X-Ray CT analysis is available) is a cylinder of 3.42 mm in diameter and 3.46 mm in width, which gives a 3.90 mm volume-based particle diameter (i.e. the diameter of a sphere with the same volume as one of the pellets is 3.90 mm). To model this experiment a 44.5 mm inner diameter cylindrical container has been filled with two thousand ceramic pellets. The A38 pellet was simulated with different numerical discretisations, from 48 to 507 tetrahedra, and the cylindrical container with 29,327 tetrahedra, for a total of approximately five hundred thousand elements for the whole model. In the numerical simulations the particles are modelled as rigid bodies with a density of 2.41 g/cm^3 . In order to avoid an artificial regularity of the pack, the particles are introduced into the domain inside the container in a random irregular grid of two hundred pellets each, from a fixed height, with random orientations and zero initial velocity.

4.1. Parameter space

The experimental bulk packing density (0.591) was calculated by integrating the axial packing density profile that was obtained from the X-

Ray CT analysis [37]. In this work, one hundred and eighty simulations with values of friction coefficient in the 0.01–1.3 range and damping coefficient in the range 0.01–0.95 were then performed to inspect the best combination of these two parameters to achieve the experimental bulk packing density. The penalty term was set to a value of 3.5×10^6 and the pellets were discretised with 16 edges on their bases (CY16), as in Fig. 7(d), to ensure high accuracy in the numerical results, as demonstrated in the next sections. In Fig. 2 the grey plane corresponds to the bulk packing density that was calculated from the physical experiment. The black circles represent the bulk packing density from the numerical simulations for different combinations of the two parameters. These values were then interpolated with a degree three polynomial surface in the parameter space. The red dashed line is the interception between the experimental plane and the interpolated surface, which corresponds to the optimal combinations of friction and damping coefficients. The results show that for any given value of friction coefficient the optimal damping coefficient is unique, and vice versa. Fig. 3(a) shows that the smaller the value of friction coefficient, the less the bulk packing density is affected by a change in damping coefficient. Fig. 3(b) shows an even stronger reduction in sensitivity to a change in friction coefficient for smaller values of damping coefficient. The optimal combinations of friction and damping coefficients to represent the physical experiment of cylindrical pellet named A38 in [37] based on just the bulk packing density is shown in Fig. 4. A value of 0.55 for the friction coefficient and a corresponding value of 0.16 for the damping coefficient were then determined also taking into account published values of sliding friction and restitution coefficients for ceramic pellets [41,42]. A summary of the input parameters and mesh resolutions used in the simulations is provided in Table 2.

4.2. Penalty term sensitivity analysis

The following sensitivity analysis was performed to evaluate the sensitivity of the results to different values of the penalty term which is used in the simulation to limit the interpenetration of the pellets. Values from 3.5×10^4 to 3.5×10^6 were considered. The friction and the damping coefficient were set to a value of 0.55 and 0.16 respectively. The circular base of the pellets was discretised with 16 edges (CY16). Fig. 5(a) shows that the vertical orientation distribution is not affected by this parameter. The radial packing density distribution instead shows a small change in the propagation of the boundary effects, as shown in Fig. 5(b). This is because a small penalty term allows more

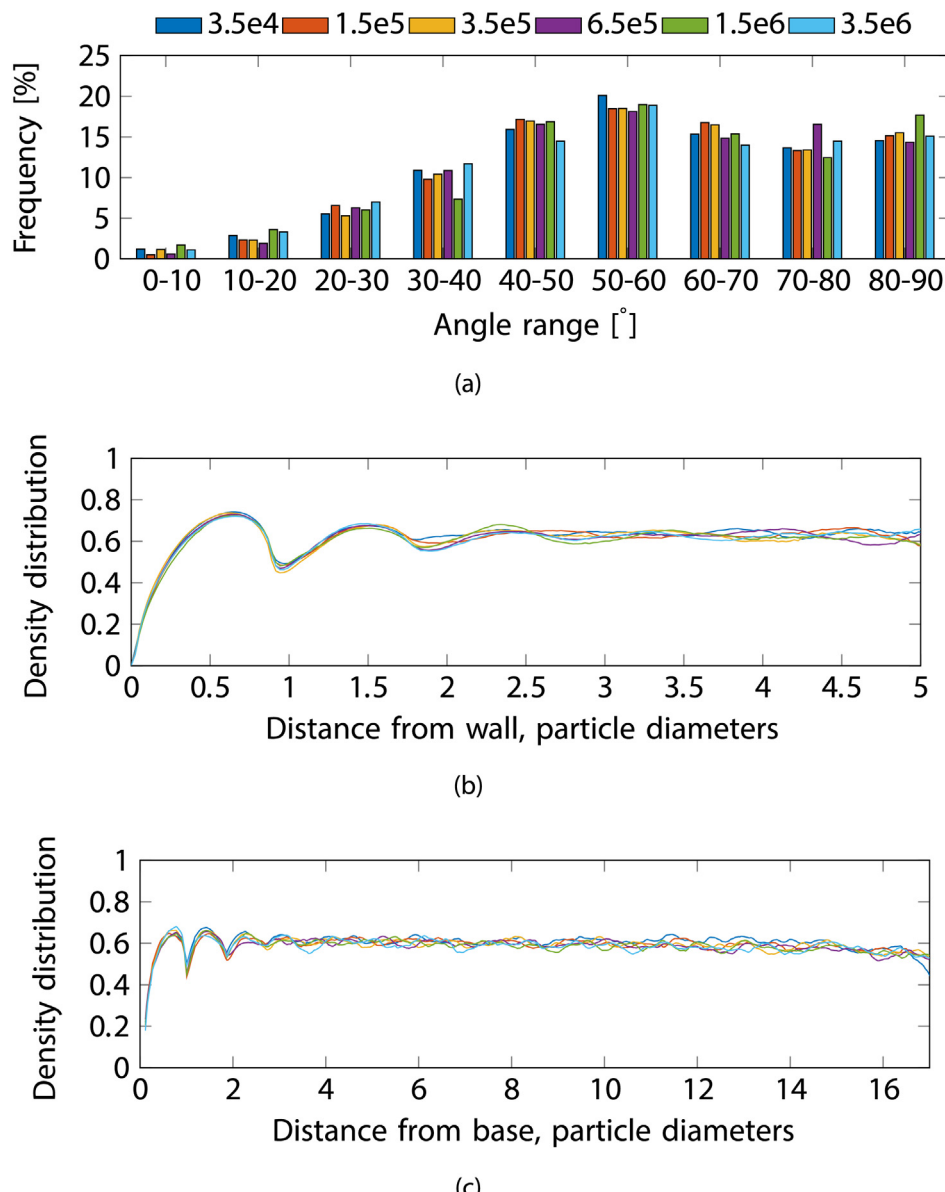


Fig. 5. Effects of the penalty term (PT) on the packing structure of cylinders in a cylindrical container: a) Vertical orientation distributions, b) radial packing density distributions and c) axial packing density distributions calculated from numerical simulations with different values of penalty term [CY16 - FC 0.55 - DC 0.16].

interpenetration between the pellets, effectively reducing their sizes. At the same time, the higher interpenetration associated with small penalty terms, reduces the effective solid volume in the pack. Moreover, Fig. 5(c) shows that the total height of the pack of 2000 pellets decreases

when reducing the penalty term, as a result of the increase in interpenetration. In Fig. 6 the effects of the penalty term on the bulk packing density has been extended to a larger value ($PT 1.5 \times 10^7$) to show the convergence behaviour in more detail and that the bulk packing

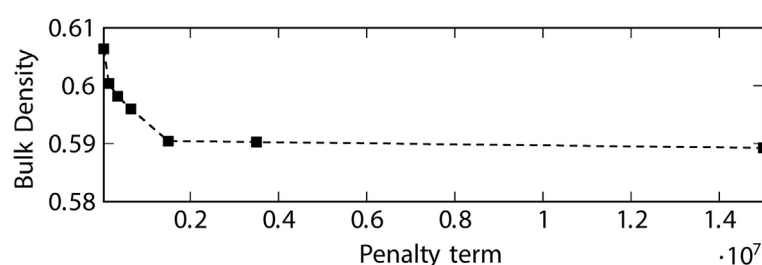


Fig. 6. Effects of the penalty term (PT) on the bulk packing density of cylinders in a cylindrical container. Bulk packing densities calculated from numerical simulations with different values of penalty term [CY16 - FC 0.55 - DC 0.16].

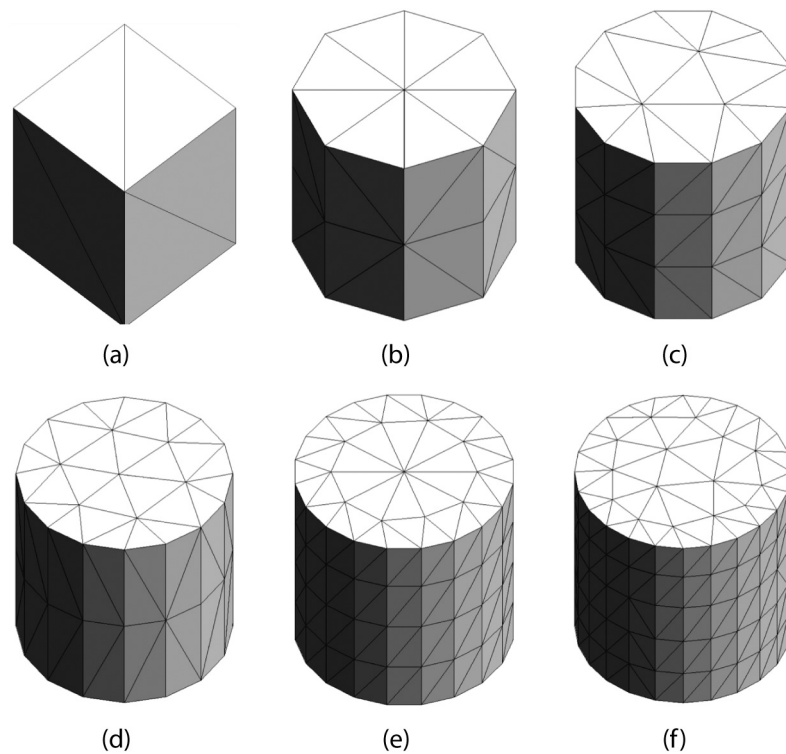


Fig. 7. Numerical mesh of cylindrical pellet named A38 as used in [37], discretised with a) 4, b) 8, c) 12, d) 16, e) 20 and f) 24 edges on its bases.

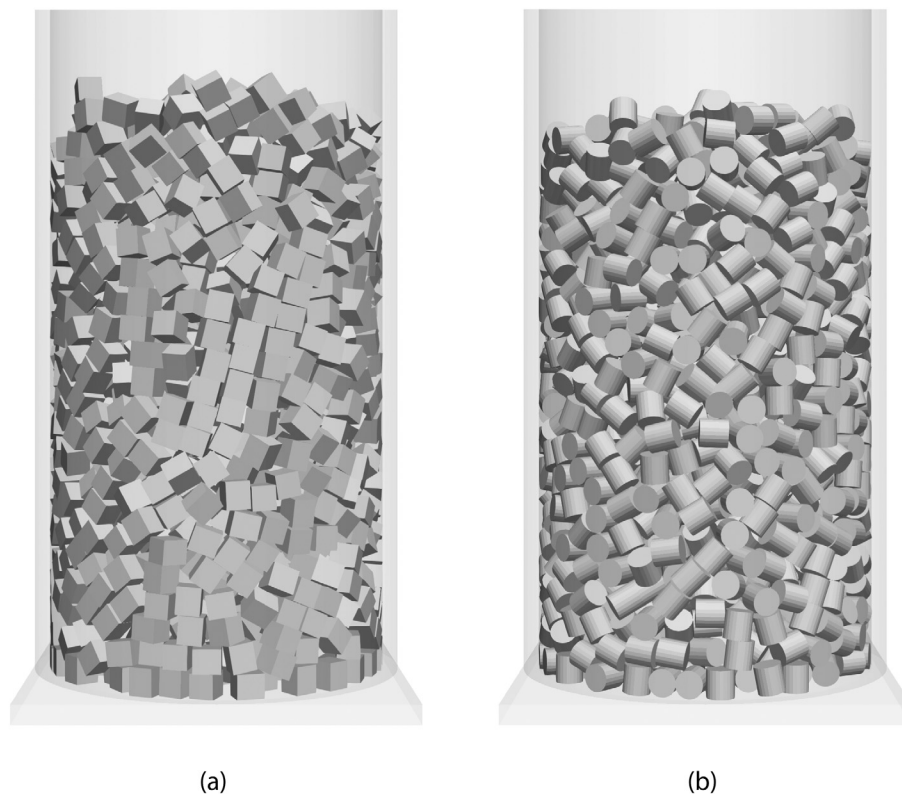


Fig. 8. Final simulated packing structures of cylindrical pellets for two mesh resolutions: a) CY04 and b) CY24.

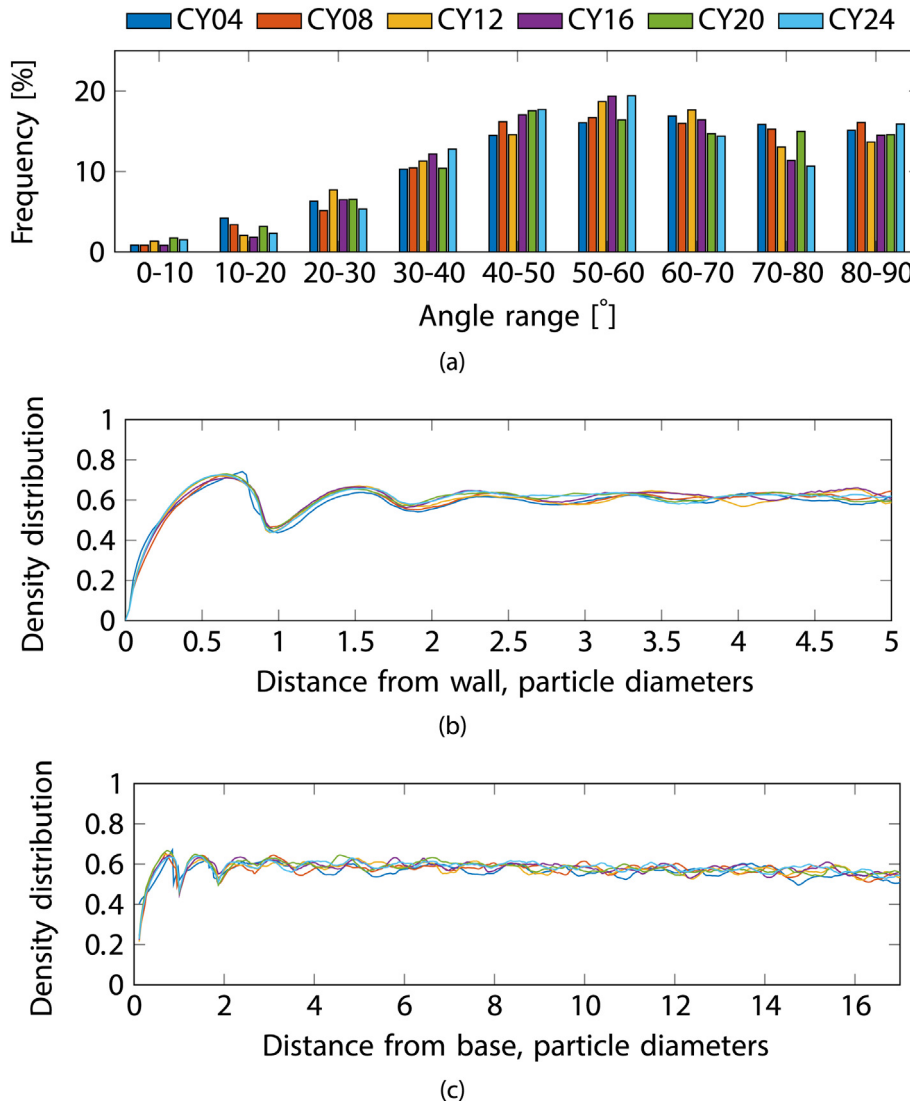


Fig. 9. Effects of the mesh resolution on the packing structure of cylinders in a cylindrical container: a) Vertical orientation distributions, b) radial packing density distributions and c) axial packing density distributions calculated from numerical simulations with different pellet meshes [PT 3.5×10^6 - FC 0.55 - DC 0.16].

density converges to a value of 0.59 for penalty terms that are larger than 1.5×10^6 .

4.3. Mesh size sensitivity analysis

This analysis was performed to evaluate the sensitivity of the results to different resolutions of the mesh of the cylindrical pellet in [37]. Pellets were discretised with 4, 8, 12, 16, 20 and 24 edges on their bases, as

shown in Fig. 7. The six meshes have the same height and base surface area, in order to maintain an identical volume to the cylindrical pellet named A38 in [37]. The penalty term and the damping coefficient were set to a value of 35×10^5 and 0.16 respectively. The friction coefficient was set to a value of 0.55. The final simulated packing structures for two different mesh resolutions (CY04 and CY24) are shown in Fig. 8 (a) and Fig. 8(b) respectively. Fig. 9(a) shows that the vertical orientation distribution is not affected by the change in the pellet mesh. The

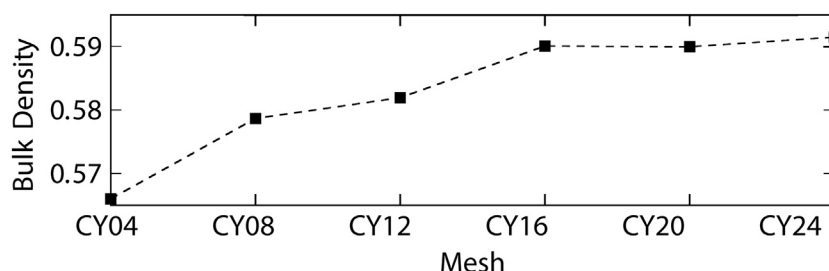


Fig. 10. Effects of the mesh resolution on the bulk packing density of cylinders in a cylindrical container. Bulk packing densities calculated from numerical simulations with different pellet meshes [PT 3.5×10^6 - FC 0.55 - DC 0.16].

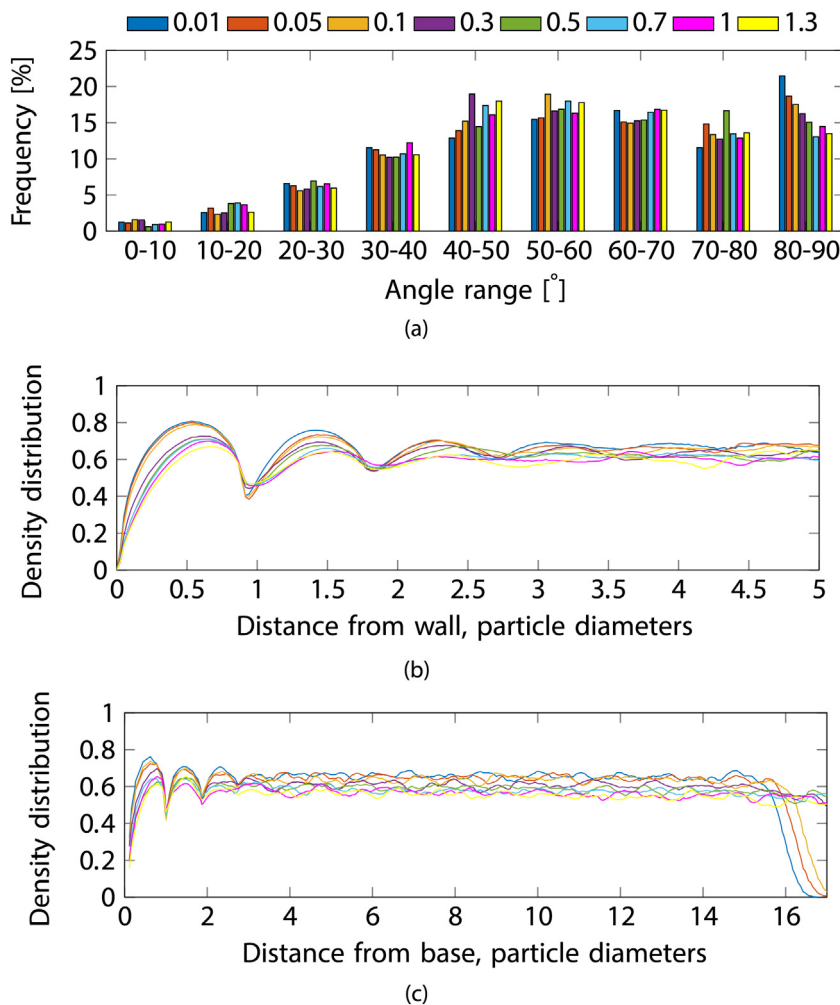


Fig. 11. Effects of the friction coefficient (FC) on the packing structure of cylinders in a cylindrical container: a) Vertical orientation distributions, b) radial packing density distributions and c) axial packing density distributions calculated from numerical simulations with different friction coefficients [CY16 - PT 3.5×10^6 - DC 0.16].

radial and axial packing density distribution, as shown in Fig. 9(b) and Fig. 9(c) respectively, show a change in the first peaks, due to the cube like pellet shape. Moreover, the axial packing density profile associated with this six-sided pellet (CY04) is on average slightly lower than the ones of the other pellets. This effect may be associated with the greater void space left between cube-like pellets that don't have enough energy to reach a more ordered packed structure (e.g. flat against flat). By reducing the damping and friction coefficients or vibrating the system this shape will generate a denser pack. Fig. 10 shows that the bulk packing density converges to a value of 0.59 for cylinders with a number of edges greater or equal to 16.

4.4. Friction coefficient sensitivity analysis

This sensitivity analysis was performed to evaluate the sensitivity of the packing results to different values of the friction coefficient. The frictional interaction between each pellet is computed with a Coulomb coefficient of friction in the 0.01–1.3 range. The penalty term and the damping coefficient were set to a value of 3.5×10^6 and 0.16 respectively. Fig. 11(a) shows that the vertical orientation distribution is affected by the friction coefficient. The lower the value of friction, the higher the tendency for the axis of the pellets to be horizontal (80°–90°), which is the most stable configuration. The radial packing density

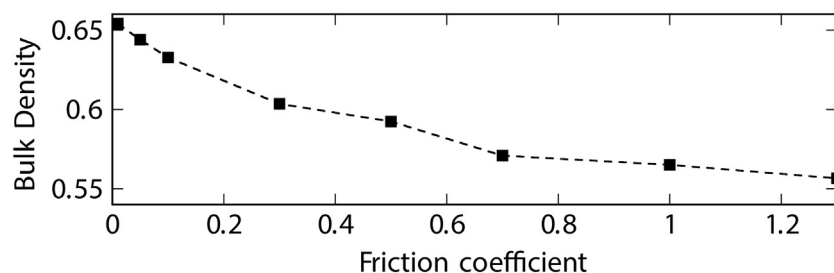


Fig. 12. Effects of the friction coefficient (FC) on the bulk packing density of cylinders in a cylindrical container. Bulk packing densities calculated from the numerical simulations with different friction coefficients [CY16 - PT 3.5×10^6 - DC 0.16].

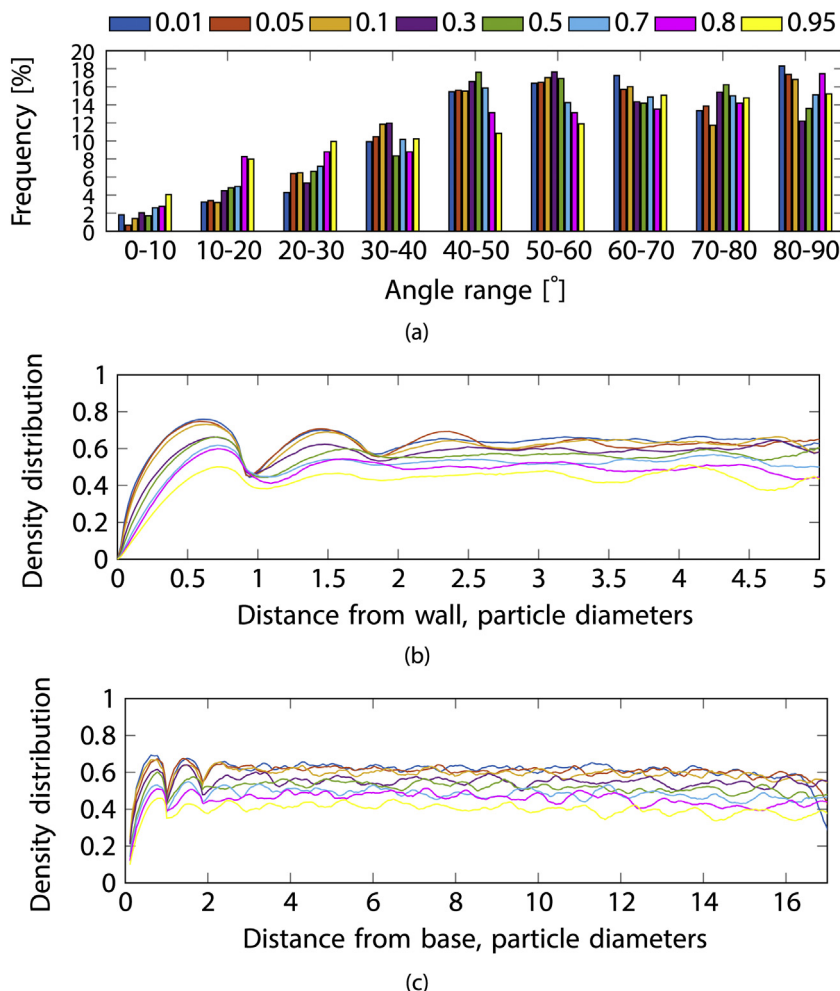


Fig. 13. Effects of the damping coefficient (DC) on the packing structure of cylinders in a cylindrical container: a) Vertical orientation distributions, b) radial packing density distributions and c) axial packing density distributions calculated from with different damping coefficients [CY16 - PT 3.5×10^6 - FC 0.55].

distribution shows a change in the propagation of the boundary effects, as shown in Fig. 11(b). This is because by reducing the friction coefficient the pellets retain more kinetic energy to reduce the voids by reaching a more ordered, dense and lower potential energy

configuration. The regularity of these configurations is represented by a larger number of peaks in packing density for multiples of the particle diameter. Fig. 11(c) shows that the total height of the pack of 2,000 pellets increases when increasing the friction coefficient, as a result of the

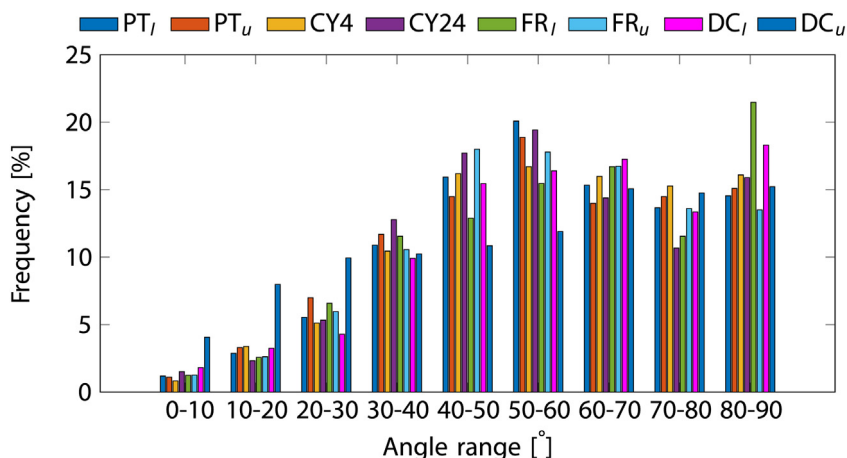


Fig. 14. Vertical orientation distributions for the lower and upper bounds of penalty term (PE_l and PE_u), mesh discretisation (CY4 and CY24) friction coefficient (FR_l and FR_u) and damping (DC_l and DC_u). The fixed parameters for each pairing in this plot are taken from the appropriate converged PE of 3.5×10^6 , converged mesh resolution of CY16, FR of 0.55 and calibrated DC of 0.16.

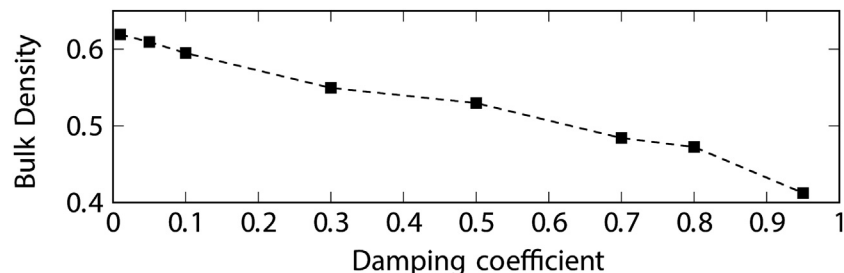


Fig. 15. Effects of the damping coefficient (DC) on the bulk packing density of cylinders in a cylindrical container. Bulk packing densities calculated from the numerical simulations with different damping coefficients [CY16 - PT 3.5×10^6 - FC 0.55].

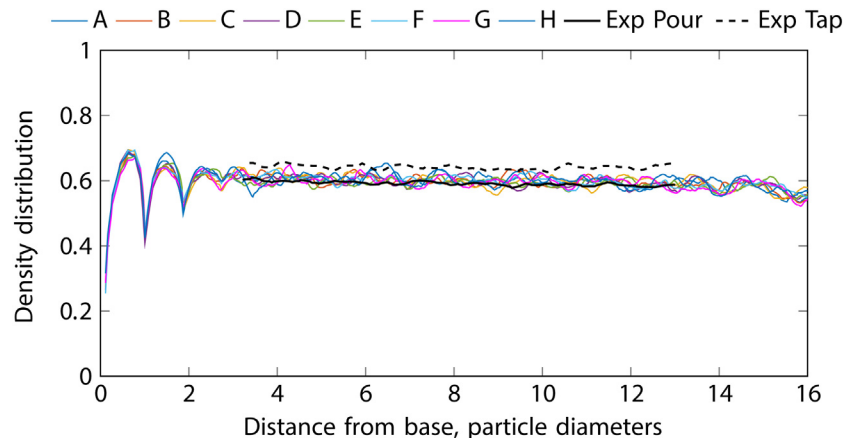


Fig. 16. Axial packing density distributions: data calculated from the X-Ray CT scans after pouring (continuous black) and after tapping (dashed black) in [37]. Data calculated from the numerical simulations of cylindrical catalysts with different seeding for the initial random location and orientation [CY16 - PT 3.5×10^6 - FC 0.55 - DC 0.16].

increase in void space between pellets. Fig. 12 shows that the bulk packing density is less sensitive to an increase in friction coefficient for values above 0.6.

4.5. Damping coefficient sensitivity analysis

The following analysis was performed to evaluate the sensitivity of the packing results to the damping coefficient. The energy loss due to the impacts between pellets and the container walls was computed with a damping coefficient in the 0.01–0.95 range. The penalty term and the friction coefficient were kept to a value of 3.5×10^6 and 0.55

respectively. Fig. 13(a) shows that the higher the value of damping, the more all the orientations became equally likely.

A comparison of the vertical distributions for the lower and upper bounds of penalty term (PE_l and PE_u), mesh discretisation (CY4 and CY24) friction coefficient (FR_l and FR_u) and damping (DC_l and DC_u) is shown in Fig. 14. The adjacent bar pairs for the extremes of PT show remarkably little difference in orientation distributions, the converged PT value adopted for the main study being near to the upper value. The adjacent bar pairs for extremes of mesh discretization suggest that only in the 70°–80° angle interval is there a marked tendency for the cube-like particle to orientate noticeably differently to the smooth cylinder for

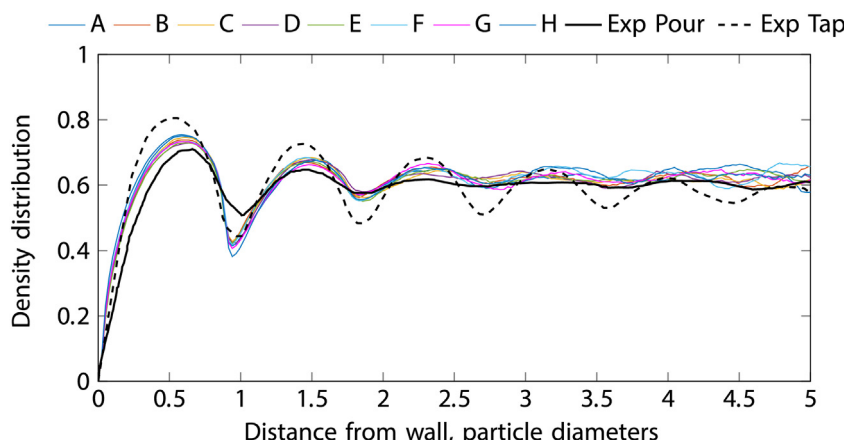


Fig. 17. Radial packing density distributions: data calculated from the X-Ray CT scans (in black) from [37], and from the numerical simulations of simple cylindrical catalysts with different seeding of the the initial random locations and orientations [CY16 - PT 3.5×10^6 - FC 0.55 - DC 0.16].

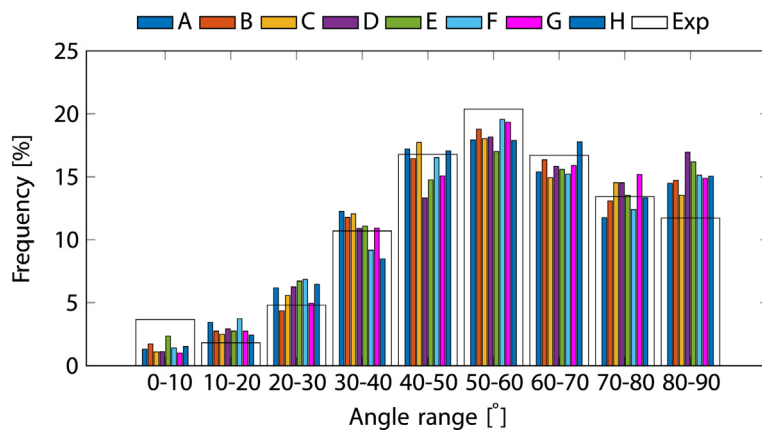


Fig. 18. Vertical orientation distributions calculated from the X-Ray CT scans from the poured experiment (in black) from [37], and from the numerical simulations of simple cylindrical catalysts with different seeding of the initial random locations and orientations [CY16 - PT 3.5×10^6 - FC 0.55 - DC 0.16].

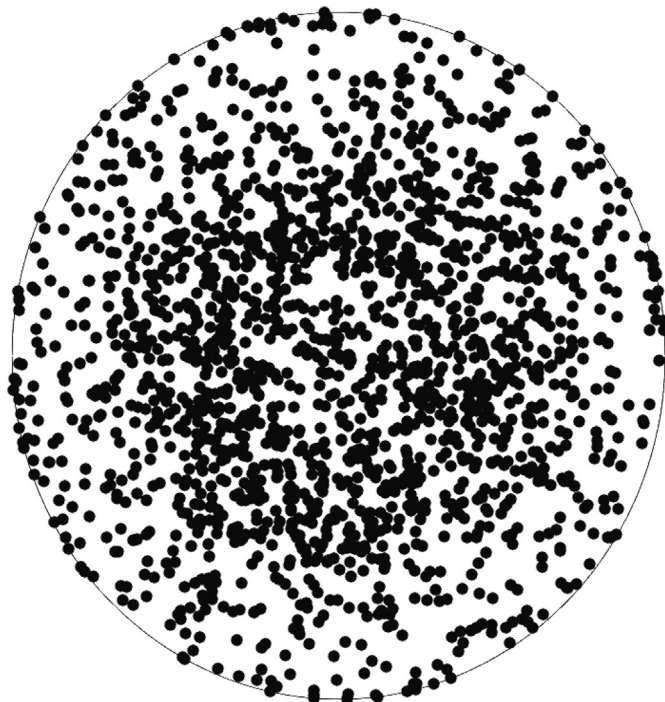


Fig. 19. Equal Angle stereographic projection representing the pellet axis orientations of the pack (Model D) for numerical simulations of simple cylindrical catalysts. Note the sparse number of dots near the centre which represents the subvertical (0–10 degrees) cylinder axes, with many more dots representing subhorizontal axes near the perimeter 80–90 degrees [CY16 - PT 3.5×10^6 - FC 0.55 - DC 0.16].

this realistic friction value of 0.55. As discussed above, for the friction parameters that extend well beyond realistic values to survey friction effects, the extreme pairing of 0.01 and 1.3 shows up marked differences in two angle intervals. For the near frictionless pellets, nearly 5% fewer occur in the 40°–50° angle range whereas about 8% more pellets settle down to the near horizontal 80°–90° angle range, reflecting the latter's lower energy state. Interesting too are the marked differences observed for the damping coefficient pairing of 0.01 to 0.95 in the low angle ranges 0°–10°, 10°–20° and even 20°–30°, where it is clear that the extremely high damping coefficient allows the final pack to retain many more (5%) of the near vertical attitudes that were fed from the original domain entry random distribution, for the case of a realistic friction coefficient of 0.55.

The radial packing density distribution, as shown in Fig. 13(b), exhibits a change in the propagation of the boundary effects, as a consequence of damping. Similarly to a reduction in friction coefficient, when reducing the damping coefficient the pellets have more energy to reduce the voids by reaching a more ordered configuration. Fig. 13(c) shows that by increasing the damping coefficient, as a result of the increase in void space between pellets, the average axial packing density decreases. A comparison between Fig. 15 and Fig. 12 for the parameter range investigated Fig. 15 shows that the bulk packing density is more sensitive to an increase of the damping coefficient than friction coefficient.

4.6. Comparison with experimental results

The axial packing density profiles that have been calculated for the numerical simulations for the packing of the A38 catalyst supports have been plotted with the corresponding curve obtained from the X-

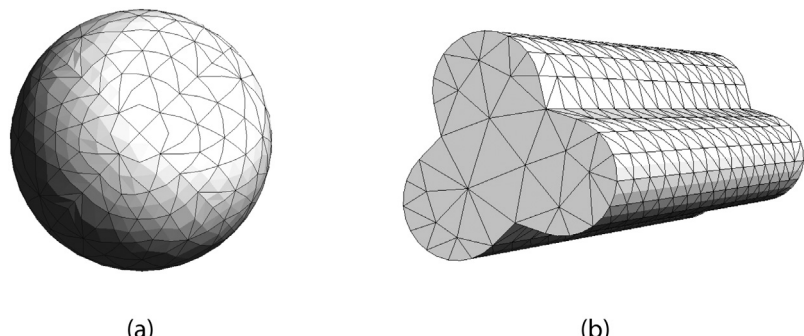


Fig. 20. Numerical discretisation of particle geometry a) spherical glass bead and b) trilobe ceramic pellet as used for the experiments in [39].

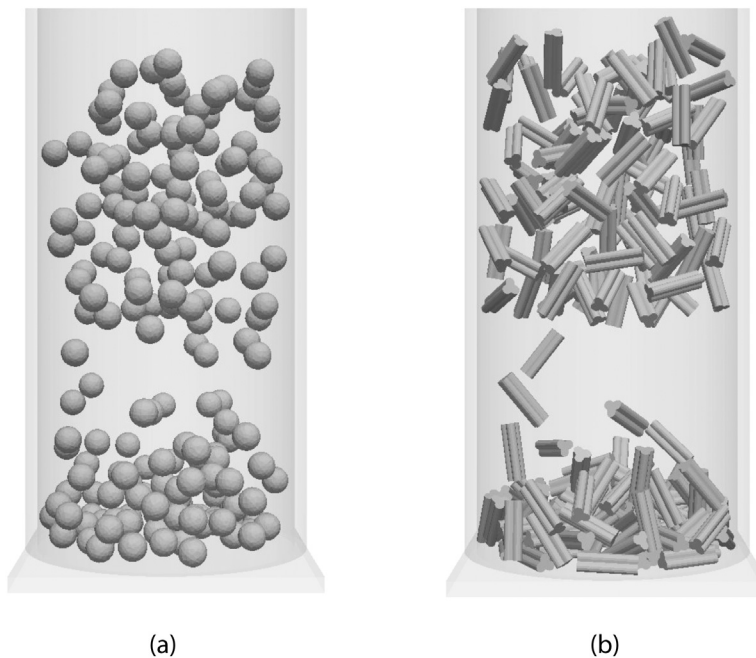


Fig. 21. Deposition process for the simulated packing structures of the two particle geometries: a) glass beads and b) trilobe pellets.

Ray CT scans in Fig. 16. To explore the repeatability from separate realisations with identical input parameters, eight simulations, corresponding to different seeding of the initial random location and orientation have been compared to the experimental results. The standard deviation for the bulk densities that were calculated from these eight tests [0.5886 0.5824 0.5824 0.5897 0.5821 0.5898 0.5874 0.5903] is equal to 0.0037. Therefore the standard deviation is about 0.625% of the mean (0.5866), i.e. a low coefficient of variation. Due to experimental constraints, the profile that has been reported in [37] represents the axial packing density from 3 to 13 particle diameters only. Because of this, it has not been possible to compare the wall effects at the bottom of the container that have been captured by the FDEM simulations

with the experimental curve. The numerical results for the axial packing density are in agreement with the corresponding experimental results from the X-Ray CT scans (black continuous line). The results in [37] also provide the packing density profiles after a vibration (tapping) has been applied to the pack of pellets (black dashed line). The vibrations allow the pellets to reduce the void space and readjust in a denser and more ordered configuration. The fact that the simulated profiles present a higher amplitude and a frequency close to the particle size when compared to relatively flat experimental profiles (even after vibration) suggests that the calculation of the density profile is more sensitive in the simulation than the one used for the experiments. Moreover, the numerical results for the particle deposition (i.e. without

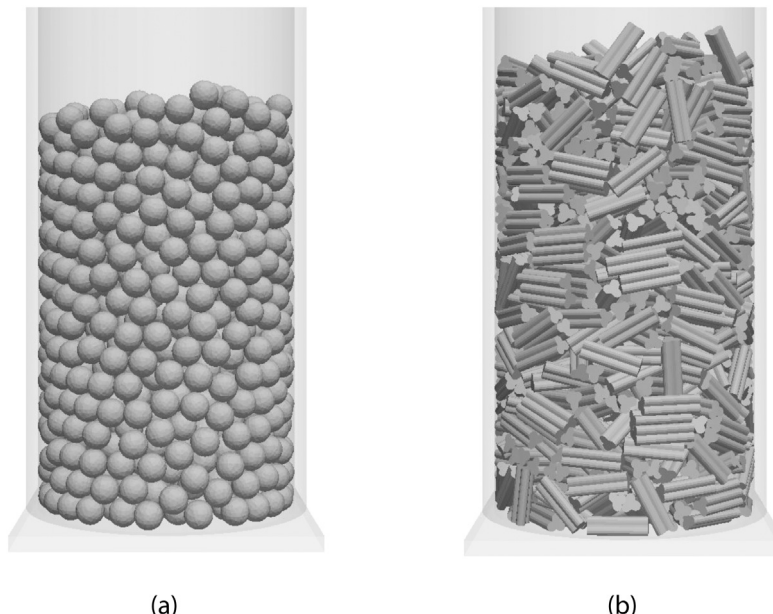


Fig. 22. Final simulated packing structures of the two particle geometries; pack of a) glass beads and b) trilobe pellets.

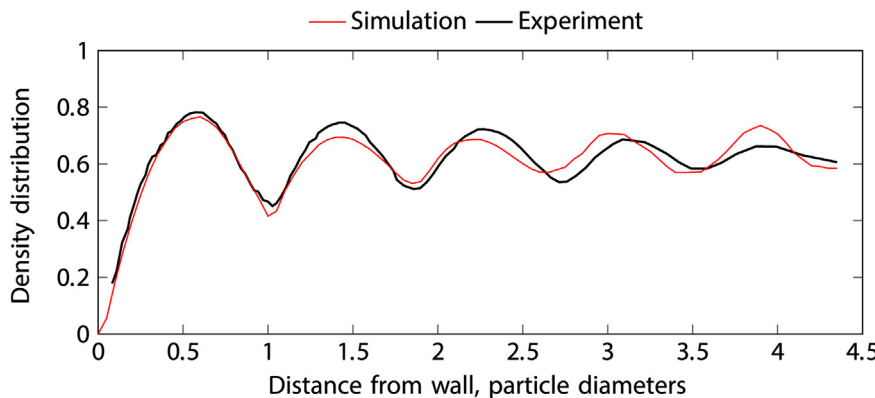


Fig. 23. Packing density fluctuations for spheres: radial packing density distributions calculated from the X-Ray CT scans (in black) from [38], and from the numerical simulations (red) [Spheres - PT 3.5×10^6 - FC 0.1 - DC 0.16]. (For interpretation of the references to colour in this figure legend, the reader is referred to the web version of this article.)

vibration) are below the experimental axial packing density after tapping, confirming the fidelity of the simulated pack.

The radial packing density profiles in Fig. 17 also show a good match between the numerical and the experimental results. The numerical results seem to have a higher amplitude periodicity in the simulated pack when considering the region 0.5 and 1.5 particle diameters from the container wall. In this region the numerical results are closer to the vibrated pack (black dashed line) than the deposited pack (black continuous line). This could be an effect of possible differences in the loading i.e. particle entry conditions that have not been reported in [37], such as the dropping height, the number per batch and the way the particles have been dropped inside the container, i.e. already having acquired a non-random orientation due to the pouring mechanism etc. Another possible cause might be the simulation boundary conditions. The container walls are fixed in the numerical simulation but free to move in the real experiment. Some of the energy might be dissipated through small vibrations of the container in the real experiments. It is not clear whether the expected slight excitation of the walls occurring in the real dynamic experiment would enhance wall effect ordering compared to the static constraint in the simulation or whether this energy transferred to the cylinder walls is simply reducing the energy available for the neighbouring particles to reach more ordered configurations.

The statistics of the pellet orientations for the angle between the axes of the cylindrical pellets and the vertical axis of the container were calculated in [37] from their X-Ray CT scans. The corresponding numerical simulations of the A38 catalyst support pack are shown in Fig. 18. The key differences are that the simulations show slightly more sub-horizontal and slightly fewer sub-vertical cylinder axes with

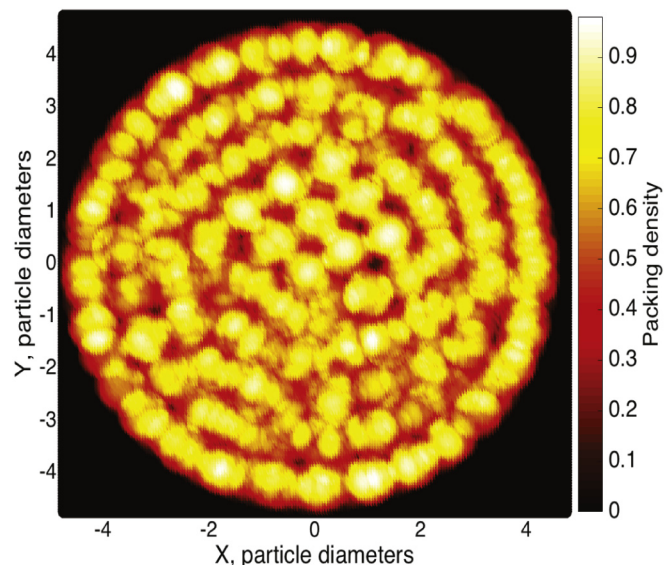


Fig. 25. Variation of packing density for spheres: average packing density perpendicular to the axis of the container as sampled within each x,y location as described in Section 6 [Spheres - PT 3.5×10^6 - FC 0.1 - DC 0.16].

the simulations also showing slightly more mid-range (40–70 degree) axes pellets. Given the uncertainties in being able to match Caulkin et al.'s experimental procedure for "pouring into the container a handful at a time" and adding pellets at the same coalescence rate, until such

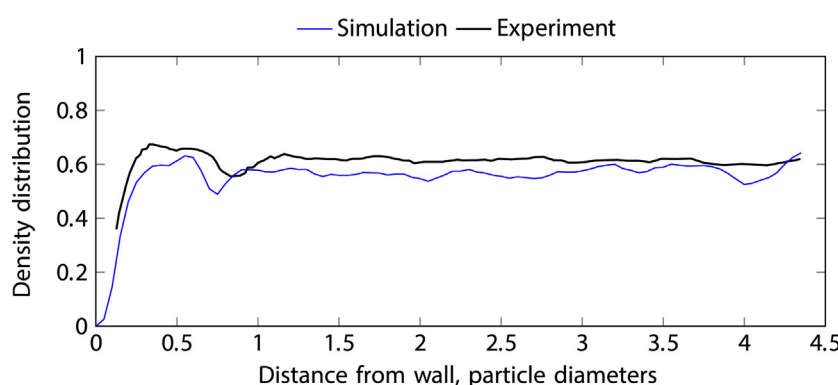


Fig. 24. Packing density fluctuations for trilobes: radial packing density distributions calculated from the X-Ray CT scans (in black) from [38], and from the numerical simulations (blue) [Trilobes - PT 3.5×10^6 - FC 0.55 - DC 0.16]. (For interpretation of the references to colour in this figure legend, the reader is referred to the web version of this article.)

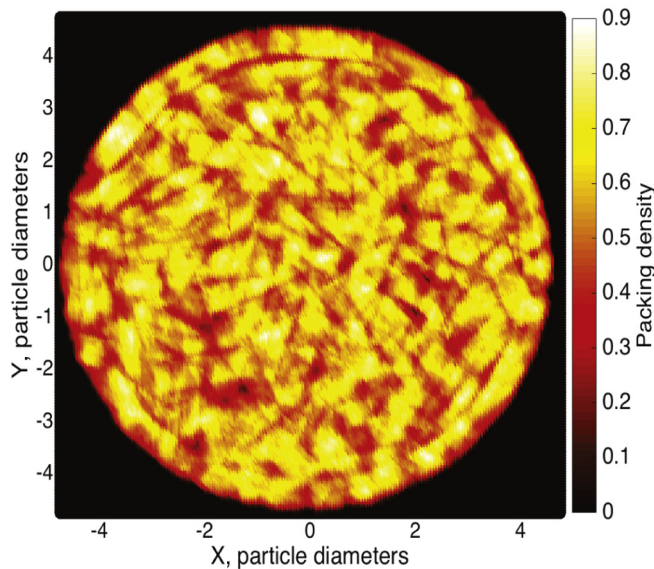


Fig. 26. Variation of packing density for trilobes: average packing density perpendicular to the axis of the container as sampled within each x,y location as described in Section 6 [Trilobes - PT 3.5×10^6 - FC 0.55 - DC 0.16].

time that more controlled packing tests can be performed together with XRay CT analysis, the numerical results for axis inclinations are considered in general terms to be in close agreement with the Caulkin experimental distributions. Needless to say, many speculative explanations can be offered for these small differences. One might be that the ‘handful’ batches are nominally entering more densely with more neighbour contacts than in the simulation’s deposition process, hence constraining the experimental packs to retain their pseudo random initial distributions to a greater extent than the slightly freer simulated deposition process. The experiments would in this case tend to inhibit the rotational freedom to a greater degree during collision impact compared to the case for the simulations. The slightly greater freedom from a supposedly less dense feed in the simulations will allow the particle’s shortest dimension axis to rotate more easily towards the upwards facing direction which typically has lower potential energy.

The stereographic projections representing the pellet orientations of one of the four numerical simulations is shown in Fig. 19. Since the experimental statistics for the pellet axis azimuth angles have not been provided in [37], it has not been possible to make a comparison for this data set. However, it is interesting to comment on the stereographic projection pattern which suggests some qualitative differences confirming what is already seen in Fig. 18, i.e., the large proportion of

pellets with axes inclined at about 40° - 70° to the vertical axis of the container. To derive the same data from the stereoplot as presented in the histogram plots, the frequency within each 10° bin would be derived by counting all the points in each concentric circular strip, progressing from the inner (0° - 10°) circle to the outer (80° - 90°) strip which has a much greater area. The point density variation seen in the stereoplot needs to be interpreted in the realisation that if all inclinations are equally represented, there would be a very dense dark cloud of points at the centre with progressively sparser point density as the perimeter is approached. The relative sparsity in the centre is therefore a very profound lack of near vertical pellets.

5. Packing of spheres and trilobes

A 19 mm inner diameter cylindrical container has been filled first with two thousand glass beads and then with one thousand six hundred ceramic trilobes. The spheres that have been packed have a diameter of 2 mm. Trilobes are catalyst supports with a base of approximately 1.3 mm in diameter and 4 mm in width, which gives a 2 mm volume-based particle diameter, see Table 1. As shown in Fig. 20(a) and (b), each sphere is discretised with 1,372 tetrahedra and each trilobe with 2,190 tetrahedra, for a total of approximately two million and seven hundred thousand elements for the whole pack of trilobes. In the numerical simulations the particles are modelled as rigid bodies with a density of 2.5 g/cm^3 . The interaction between each pellet is computed with a Coulomb coefficient of friction of 0.1 for the glass beads and 0.55 for the trilobes. The damping coefficient employed to represent the energy loss due to the impacts is 0.16. The values of sliding friction and damping (e.g. restitution coefficient) were not provided in [38]. For this reason an informed guess of these two parameters was made with a parametric study, taking into account the values for glass and ceramics that are generally reported in the literature. With a similar procedure adopted for the cylindrical catalyst deposition, in order to avoid imposing an artificial regularity on the pack, the spheres and trilobes are introduced into the domain above the container base in a random irregular grid of one hundred pellets each, from a fixed height, with random orientations and zero initial velocity, as shown in Fig. 21 (a) and (b) respectively.

The simulation results corresponding to the two particle shapes, as shown in Fig. 22, have been compared to experimental results, but this time only the experimental radial packing density profiles were reported in [38]. Because of this, it has not been possible to compare the axial packing density profiles and particle axis orientations calculated from the simulations to the correspondent experimental data. The radial packing density profiles in Fig. 23 show a good match between the numerical and the experimental results for the pack of glass beads. Moreover, the periodicity of the boundary effects is well represented by the numerical simulation, showing five distinctive peaks in the density

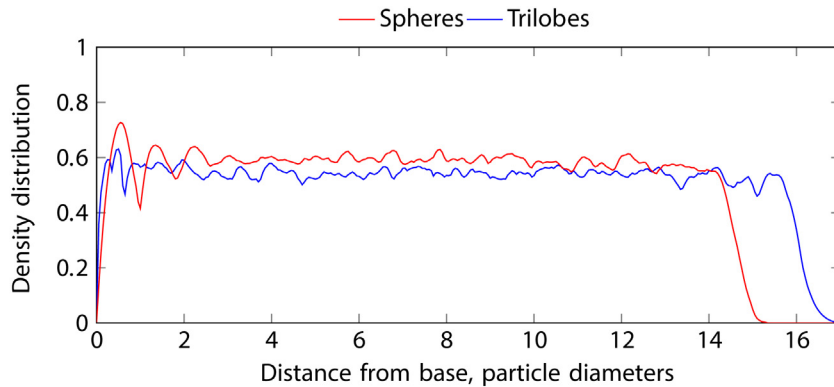


Fig. 27. Axial packing density variations calculated as derived from the numerical simulations of spheres (red) and trilobes (blue) in a cylindrical container. (For interpretation of the references to colour in this figure legend, the reader is referred to the web version of this article.)

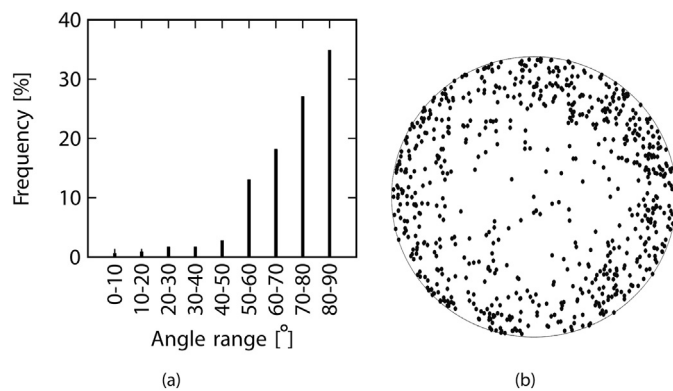


Fig. 28. a) Orientation distribution derived from the numerical simulations of packing of trilobes in a cylindrical container. b) Stereographic projections representing the pellet orientations as derived from the numerical simulations of packing of trilobes in a cylindrical container [Trilobes - PT 3.5×10^6 - FC 0.55 - DC 0.16].

distribution profile. The radial packing density profiles in Fig. 24 show almost as good a match between the numerical and the experimental results for the pack of trilobes, with the simulated density marginally lower. In this case, both the experimental and numerical results have a single drop in the radial profile between 0.5 and 1 particle diameters from the container walls, suggesting that the boundary effects are limited to the proximity of the container. This difference in the pack structure for the two particles can be found also when comparing the average packing density perpendicular to the axis of the container calculated from the numerical simulations. In Fig. 25 the glass beads are arranged in concentric rings that propagate from the wall to the centre of the container. For trilobes, the periodicity away from the wall cannot be maintained. In Fig. 26 the trilobes make just one ring in proximity of the wall, resulting in a less ordered packing structure for the inner part of the container. This difference in the order of the packed structure for the two particle geometries could be explained as follows. For each possible location that a particle may assume, the number of all the possible stable configurations that are available for a trilobe pellet (i.e. all the possible orientations that are allowed by the neighbouring particles) is much larger if compared to the only possible stable configuration of a sphere, since all the orientations of a sphere are equivalent due to its symmetry. For this reason, while the container wall effects are propagated through the whole pack by the spheres, the trilobe pellets attenuate the boundary effects due to their much larger degree of freedom. In Fig. 27 the axial packing density profile calculated from the numerical results of the pack of glass beads is compared to the one obtained from the simulation of trilobes. Again, the boundary effects are much more pronounced in the pack of spheres, with four distinctive peaks in the proximity of the container base. Both profiles have a gentle negative slope, representing the higher compaction of the deeper layers of particles as determined by the over-burden mass of the particles above, as shown in the case of cylindrical pellets in the previous sections. Fig. 28 (a) shows the statistics of the trilobe orientations for the angle between the axis of the pellet and the axis of the container that have been extracted from the numerical simulations. Due to the large aspect ratio of these particles, the configurations nearer to vertical (from 0° to 50°) are unstable upon first contacts and therefore the trilobes in the pack structure are mostly in the sub-horizontal orientations. This is in stark contrast to the cylinders shown in Fig. 18. The cylinders simulated in the previous Section had an aspect ratio close to one, which encouraged the stability orientations to be more widely distributed and to include virtually all angles including close to the vertical. This difference is expressed very clearly in the stereographic projections for the cylinders in Fig. 19, which are scattered across all orientations throughout the whole domain, whereas for the trilobes in Fig. 28, they tend to occupy

the outer region of the plot, representing the sub-horizontal configurations.

6. Conclusions

The effects on the bulk properties of rigid cylindrical pellet packs of mesh resolution, friction, energy dissipation and other numerical parameters have been presented and discussed. The optimal parameters for the simulation of the A38 cylindrical catalyst supports in [10] have been inferred by means of a sensitivity analysis using the mesh resolution and penalty term values that have been shown to be sufficiently converged, and by studying the parameter space to find valid pairings for the friction and damping coefficients. Experimental and numerical axial and radial packing density profiles and orientation distributions have been compared, confirming that the FDEM numerical simulations of packing of rigid A38 cylindrical catalyst supports, glass beads and trilobe pellets deposited in a cylindrical container match the corresponding emergent bulk properties obtained from X-Ray CT scans within very encouraging limits. These results give a first confirmation of the capabilities of the FDEM based code Solidity for the simulation of packed structures of catalysts in fixed-bed reactors. The results in this work also constitute a necessary step towards future studies with coupled FDEM formulations involving hydro-thermo-mechanical, fracturing and fragmentation interactions of catalysts in fixed-bed reactors. It will also allow the representation of more realistic loading conditions and deformable material responses that can lead to the crushing of catalyst supports for future extensions of the work employing the deformable FDEM code as presented in [31]. In the present work the fidelity of the pellet skeleton topology output from the rest state of the FDEM simulations has been assessed by means of emergent bulk properties such as axial and radial packing density profiles, orientation distributions, etc. It is anticipated that more confirmation of the high degree of accuracy of the packing structures that are generated with FDEM will be obtained in future work when comparing other mechanical properties of the pack. For example, the simulated values of pressure on the container walls can be compared with the pressure results from actual packing experiments. Another interesting prospect is to simulate the effects on packing structures of different aspect ratios in packs of cylindrical pellets or other geometric forms. More research also needs to be carried out to study the relation between the history of particle entry, such as hopper feeds, hand-batches, custom made feed regulator (e.g. unidense), with the properties of final packed structures.

Declaration of Competing Interest

The authors declare no competing financial interests.

Acknowledgement

This research was supported by the Engineering and Physical Sciences Research Council (EPSRC) with a Case studentship in collaboration with Johnson Matthey (Ref: 1402780) and an Impact Acceleration Account grant (Ref: EP/R511547/1).

Appendix A. Axial and radial packing density profiles

The numerical results are analysed with a post-processing tool that has been specifically developed to reproduce the calculation process employed to evaluate the axial and radial packing density profiles and the pellet orientation distribution from the voxelised data format of the X-Ray CT scans that has been employed in [37,38]. A regular grid to generate an equivalent voxel structure is defined in the domain of the numerical results. A value of 1 is assigned to the centroid of the voxel cells that are inside a tetrahedron of the solid mesh and 0 is

assigned otherwise. For the sake of clarity, in Fig. 29 the cell dimension is shown here to be similar to the dimension of the pellets. The real cell dimension chosen for the calculations is less than one tenth of the element size, allowing a more precise discretisation of the packing density. The binary values of each cell are then summed and averaged within each horizontal plane from bottom to top to calculate the axial packing density profile, as shown in Fig. 30(a) and (b). The cells are then averaged along columns to obtain a planar profile of the average packing density perpendicular to the axis of the container as shown in Fig. 30(c). The values on the plane are then averaged along concentric rings to calculate the radial packing density profile, as illustrated in Fig. 30(d), from concentric halos of equal areas.

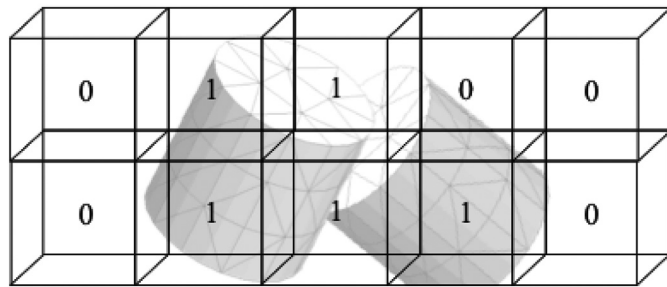


Fig. 29. Representation of the regular grid in the domain of the numerical results. Note, a much finer voxel size is actually used to calculate the solid volume fraction in each slice.

Appendix B. Vertical orientation distributions and stereographic projections

The coordinates of the axis of each pellet are calculated using the inertia tensor of the bodies that are calculated to compute the rotational effects of contact forces in the rigid FDEM simulations. This data set is exported at the end of the simulation to further characterise the packed structure. In particular, the angle between the axis of the catalyst support and the axis of the container Fig. 31(a) is employed to generate statistics of the pellet orientation distributions that are then compared with the corresponding data from the X-Ray CT scans from [37]. Lambert Equal Area lower hemispherical projections are generally used for presenting three-dimensional information on a two-dimensional plot. Stereographic projections are commonly employed in structural geology and geotechnical engineering applications [43], but they have been used also for assessing randomness and clustering of orientations of symmetry axes of concrete armour units within breakwater armour layers [44] and pharmaceutical tablets [45] orientation representation. Visual representation of the relationships between the angles of crystals are also provided by stereographic projections [46]. In Fig. 31(b) the equatorial reference frame represents the plane of the container base and the plotted pellet orientations are illustrated as they would appear from a top view. In Fig. 31(c) the stereographic projection for the orientations of a simulated cylindrical catalyst support packed structure has been shown.

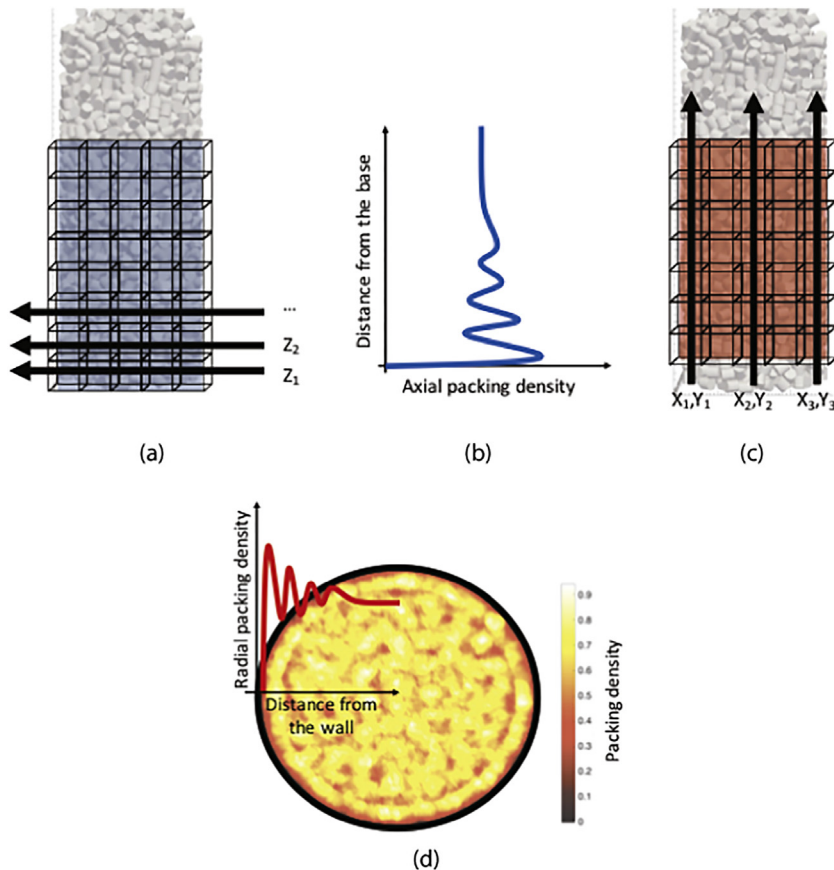


Fig. 30. a) Averaging the values of cells along horizontal planes; b) axial packing density profile, c) averaging the values of cells along vertical columns; d) visualisation of the simulated average packing density as observed perpendicular to the axis of the container together with superimposed radial packing density profile showing periodic wall effect as also seen in the visualisation.

